Supramolecular Non-Amyloid Intermediates in the Early Stages of α-Synuclein Aggregation

Jonathan A. Fauerbach,[†] Dmytro A. Yushchenko,[‡] Sarah H. Shahmoradian,[§¶] Wah Chiu,[§¶] Thomas M. Jovin,[‡*] and Elizabeth A. Jares-Erijman[†]

[†]Departamento de Química Orgánica, Facultad de Ciencias Exactas y Naturales, Universidad de Buenos Aires (UBA), CIHIDECAR CONICET, Buenos Aires, Argentina; [‡]Laboratory of Cellular Dynamics, Max Planck Institute for Biophysical Chemistry, Göttingen, Germany, and Laboratorio Max Planck de Dinámica Celular (UBA), Buenos Aires, Argentina; [§]Department of Molecular Physiology and Biophysics and [¶]National Center for Macromolecular Imaging, and Verna and Marrs McLean Department of Biochemistry and Molecular Biology, Baylor College of Medicine, Houston, Texas

ABSTRACT The aggregation of α-synuclein is associated with progression of Parkinson's disease. We have identified submicrometer supramolecular structures that mediate the early stages of the overall mechanism. The sequence of structural transformations between metastable intermediates were captured and characterized by atomic force microscopy guided by a fluorescent probe sensitive to preamyloid species. A novel ~0.3–0.6 μm molecular assembly, denoted the *acuna*, nucleates, expands, and liberates fibers with distinctive segmentation and a filamentous fuzzy fringe. These fuzzy fibers serve as precursors of mature amyloid fibrils. Cryo-electron tomography resolved the acuna inner structure as a scaffold of highly condensed colloidal masses interlinked by thin beaded threads, which were perceived as fuzziness by atomic force microscopy. On the basis of the combined data, we propose a sequential mechanism comprising molecular, colloidal, and fibrillar stages linked by reactions with disparate temperature dependencies and distinct supramolecular forms. We anticipate novel diagnostic and therapeutic approaches to Parkinson's and related neurodegenerative diseases based on these new insights into the aggregation mechanism of α-synuclein and intermediates, some of which may act to cause and/or reinforce neurotoxicity.

INTRODUCTION

The aggregation of the presynaptic 140 aa (14.5 kDa) protein α-synuclein (AS) is a prominent cytopathological feature of Parkinson's disease (PD), manifested by the deposition of dense tangles of fibrils with a characteristic amyloid cross-β-sheet secondary structure in dopaminergic neurons of the substantia nigra and related nuclei of the midbrain (1,2). Neuronal dysfunction or death due to protein aggregation is also characteristic of other neurodegenerative conditions, such as Alzheimer's disease (AD) (3). Diagnosis has relied exclusively on clinical assessment, and current therapy is palliative and temporary. Although predictive molecular markers (4) and strategies based on molecular features (5) are emerging, at this time, PD cannot be prevented or cured.

Mature amyloid fibrils of AS predominate in the Lewy bodies and Lewy neurites characteristic of PD and other synucleopathies (2). However, numerous investigations indicate that neurotoxicity may instead derive from soluble, oligomeric, "mysterious" (6) reaction intermediates (7,8). Thus, the molecular constituents of inclusion bodies (>8 proteins in the case of Lewy bodies (9)) may serve as witnesses to rather than as the cause of cell degeneration. It has been proposed that oxidative modifications, mitochondrial functional disruption, and impairment of normal protein degradation resulting from environmental exposure, genetic factors, and endogenous insults constitute a "Bermuda triangle" of neurodegeneration (10).

Numerous fluorescent probes are applied in studies of amyloid aggregation (11,12). Unfortunately, organic compounds such as thioflavin T (ThT), which is used to demonstrate mature amyloid fibrils in assays or in cytochemical staining, are insensitive to prefibrillar precursors. Our recent studies of AS aggregation have been based on fluorescent compounds exhibiting excited-state intermolecular proton transfer (ESIPT). Excited-state tautomerism leads to a dual emission that is extremely sensitive to local molecular features such as polarity and hydrogen bonding (13). Thus, ESIPT probes provide multiple fluorescent signals, including absolute intensities of the N* (normal) and T* (tautomer) bands, T*/N* ratio, polarization, spectral position(s), and lifetime(s). In our first application of such fluorophores we used an extrinsic dye (FE) that is able to distinguish between wild-type (wt) and familial mutant fibrillar forms of AS (14).

To explore the critical initial, elusive phases of the aggregation mechanism, we switched to covalent adducts of ESIPT probes (e.g., MFC), inserted at defined sequence positions (18, 90, 140) of functionally neutral Ala-to-Cys AS mutants (15). Mixtures of unlabeled wtAS and a low reporter concentration (~3%) of labeled protein exhibited multiple and pronounced spectroscopic changes during the early stages of AS aggregation, i.e., before the appearance of an appreciable ThT response. The effects were

Submitted November 30, 2011, and accepted for publication January 26, 2012.

Corresponding author E. A. Jares-Erijman died on Sept. 29, 2011, during the revision of the manuscript. The surviving authors dedicate this publication to her memory and in acknowledgment of her inspiration and leadership.

*Correspondence: tjovin@gwdg.de

Editor: Peter Hinterdorfer.

0006-3495/12/03/1127/10 $2.00

doi: 10.1016/j.bpj.2012.01.051

interpreted in terms of changes in polarity, hydrogen bonding, and motional constraint of the protein-attached probe, with clear distinctions between the properties of the fibrillar amyloid end state and its apparent precursors.

To establish the structural identity of the latter, we sampled the reactions at various intervals by atomic force microscopy (AFM), guided by the temporal course of the ESIPT T*/N* ratio. This evaluation led to the recognition (reported here) of a family of supramolecular entities arising and disappearing in a well-defined orchestrated sequence. We have named a key subpopulation of this family *acunas*, a contraction of the word "amyloid" and the Spanish word "cuna" (cradle in English). The term is prompted by the appearance of oval-to-round supramolecular assemblies (diameter $\geq$200 nm) upon which distinct highly segmented and laterally decorated (fuzzy) fibers nucleate, extend, and are then liberated. We have distinguished at least eight distinct molecular species by AFM.

Because AFM is exclusively a probe of surface topology, we resorted to cryo-electron tomography (cryo-ET) to investigate the inner structure of the acuna under fully hydrated conditions. Cryo-ET is a method of choice for investigating large, pleomorphic supramolecular assemblies (16–18), either in isolated form or in their cellular environment. The electron micrographs provide two-dimensional (2D) projections of a three-dimensional (3D) object that is vitrified in solution before examination. To retrieve 3D structures, we tilted the specimens with respect to the electron beam while recording a series of 2D images at different projections. We then reconstructed a tomogram of the 3D volume from the annotated stacks of image data (see Fig. 4).

Most electron microscopic and tomographic studies of biological structures rely on conventionally prepared specimens subjected to chemical fixation, staining, dehydration, and embedding. However, these procedures can result in severe structural artifacts (19,20). In contrast, cryo-electron microscopy uses specimens that are isotropically vitrified in appropriate buffers or solutions at liquid nitrogen temperature, which preserves their close-to-native conformation (21). In addition, the specimens are maintained at temperatures near −180°C during microscopy, which effectively lessens the overall radiation damage.

MATERIALS AND METHODS

AS and aggregation assays

Aggregation assays of wtAS protein in combination with cysteine-containing mutants labeled with the MFC ESIPT probe were performed at 4°C, 37°C, and 70°C as described previously (15). Procedures are described in the Supporting Material.

Atomic force microscopy

A detailed description of the AFM sample preparation and image analysis (morphological analysis approaches and procedures) is given in the Supporting Material.

Cryo-ET

Details regarding specimen preparation and Cryo-ET procedures are provided in the Supporting Material.

Image processing

Tomographic reconstruction and image processing were performed using IMOD software (22) and the EMAN2 (23) package for Linux. The tilt series was normalized via IMOD to avoid uneven distribution of intensities. Projection images (1048×1048) were aligned to a common origin, using selected areas of high contrast, and reconstructed by means of weighted back-projection via *eTomo*, a graphical user interface (GUI) to the IMOD Tomography package. The featured tomogram was binned by a factor of 2 and low-pass filtered to 100 Å using the EMAN2 software package.

Tomogram annotation

For segmentation of the reconstructed tomogram, were identified and extracted individual features, such as the beaded threads and condensed colloidal masses, in silico. We then calculated 2D images of these elements by projecting the volumes along the z axis using AMIRA 5.2 software (Visage Imaging GmbH, Berlin). Visualizations were constructed with the use of surface-rendering operations in AMIRA 5.2 software. To assist visualization, structural features were segmented from the binned, low-pass filtered tomogram with Amira Brush and Blow tools. The AS beaded threads and condensed colloidal masses were subjectively colored in a purple-to-red gradation along the z axis, and the acuna and surrounding features were subjectively colored in yellow. To ensure accurate segmentation, slices above and below each beaded thread and condensed colloidal mass in the z axis were manually tracked to verify their continuity throughout the slices. Unclear, low-contrast features lacking continuity throughout the slices were designated as noise.

RESULTS

AS aggregation and AFM

The time course of the aggregation reaction conducted at 37°C of wtAS + 2.5% A140C-MFC was monitored by means of the T*/N* ratiometric signal of the ESIPT probe and later by the ThT assay (Fig. 1 *A*). As reported previously (15), the T*/N* ratio rose, peaked, diminished, and then stabilized before the appearance of the maximal ThT response. Samples were taken for examination by AFM at the indicated times (Fig. 1, *A* and *C*). Reproducibility was obtained in the aggregation experiments by ultracentrifugation of the initial monomeric protein, resulting in ruffled film on the mica surface devoid of nano- and microaggregates (Fig. 1, *A* and *C*; Fig. 2, *A* and *B*; and Fig. S1 in the Supporting Material).

During the initial ~15 h of AS self-assembly, the system evolved into a series of oligomeric and supramolecular entities (Fig. 1 *C*.2–5), which arose and disappeared in succession. The final supramolecular product consisted exclusively of mature amyloid fibrils (*mafs*; Fig. 1 *C*.6).

At 70°C, the aggregation reaction was significantly accelerated (14) without affecting the nature and sequence of the intermediates, although the high temperature led to an apparent chemical degradation of the ESIPT probe (15).

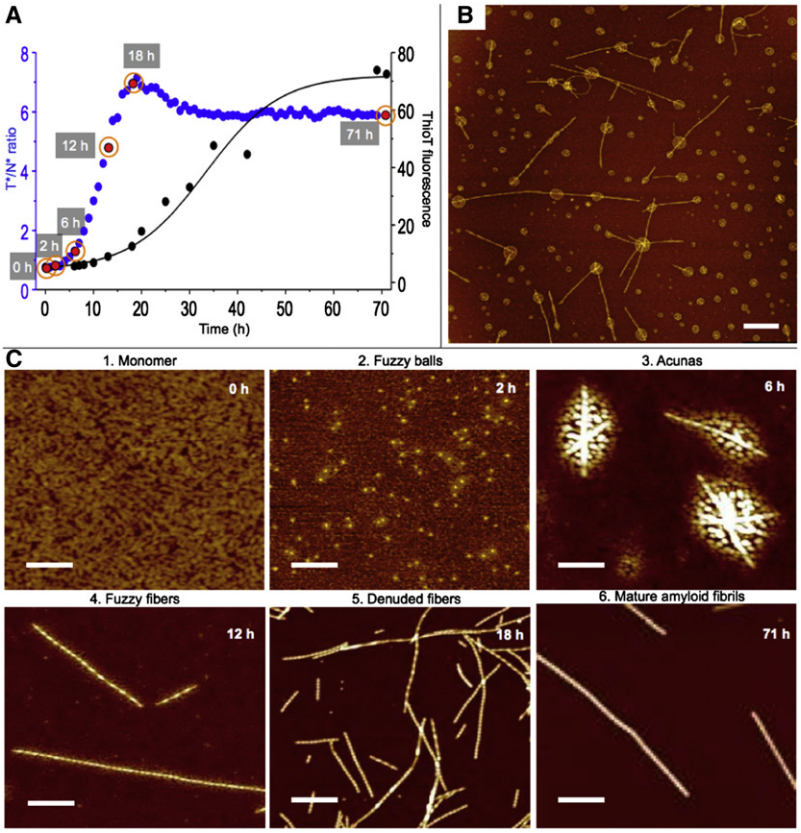

FIGURE 1 Aggregation of ESIPT-labeled AS. (*A*) Reaction at 37°C. T*/N* ratio (*blue dots*) and ThT (*black dots* and *solid fit line*). The ThT transition midpoint, $t_{1/2}$, was ~30 h. AFM sample points are shown in red. (*B*) Field with multiple acuna structures of an incubation at 70°C; image acquired at 12 h. (*C*) AFM images representative of different oligomeric species found during the course of reaction corresponding to the wtAS control sample in panel *A*. The sampling times and names (see text) are indicated in each panel. AS: wt + 2.5% AS140C-MFC (15). Scale bars: 500 nm.

An AFM image taken at 12 h revealed a heterogeneous family of intermediates (Fig. 1 *B*, Fig. S13, and Fig. S14), including acunas (see Introduction). In contrast, in reactions conducted at 4°C, there were no changes in fluorescence and supramolecular fiber-free *latent* acunas (see below) accumulated as the end product.

From the data obtained in these and numerous other highly reproducible experiments, we constructed a gallery of representative images characterizing the family of intermediates (Fig. 2). Statistical estimations of the key structural parameters (heights, diameters and periods) are given in Fig. 3. A number of conditions (color-coded) are represented in Fig. 2, including wtAS in the presence and absence of labeled protein as well as incubations at 4°C, 37°C, and 70°C with mechanical agitation (except for panels *C* and *D*). The panels of Fig. 2 feature subimages (ranging from 0.7 to 50 μm) culled from AFM scan fields of samples applied to the mica surface by spin-coating (except for panel *E*). This procedure is ideally suited for particulate and fibrillar material, which is dispersed into a thin film before drying (24) (see Supporting Material). The AS supramolecular forms were observed over and embedded within the layer of monomer, which adhered quickly and strongly to the mica. No differences were observed between the images obtained with protein with or without a labeled subpopulation.

The fuzzy ball (*fb*), the earliest perceptible structure in incubations at all temperatures (Fig. 2, *A* and *B*), is a nanosphere with a height of ~4 nm; the apparent lateral diameter (30 ± 4 nm) is dilated by convolution with the finite AFM tip diameter. The *fb* exhibits a progressive tendency to recruit material at its periphery (~1 nm height) perceived as fuzziness. Coalescing into an accretion zone with up to five round entities, the *fbs* lead to the formation of distinctive supramolecular structures, the acunas.

Acunas appear as an oblong or circular discs by AFM in air (top view), but as oblate ellipsoids by cryo-ET (Fig. 4). We attribute the collapse of the air-dried AFM samples to the loss of hydration stabilizing the tenuous internal structure preserved by the isotropic vitrification procedure of cryo-ET. Given a sufficiently high protein concentration (e.g., $\geq$200 μM), acunas form spontaneously at 4°C without agitation (Fig. 2, *C* and *D*), but are also observed at higher temperatures with agitation (Fig. 2, *E–N*). The diameters are 200–250 nm and the heights are 15–40 nm (Fig. 3). Latent acunas generated at 4°C are distinguished by a central area with discrete particles that are presumed to originate by coalescence of *fb*s (Fig. 2 *D*). At 4°C, the acunas do not proceed further in the aggregation process (attached fibers are absent; Fig. 3) and exhibit neither an appreciable fluorescent ESIPT response (increase in T* and N* band intensities; Fig. 1 *A*) nor a β-strand circular dichroism signature.

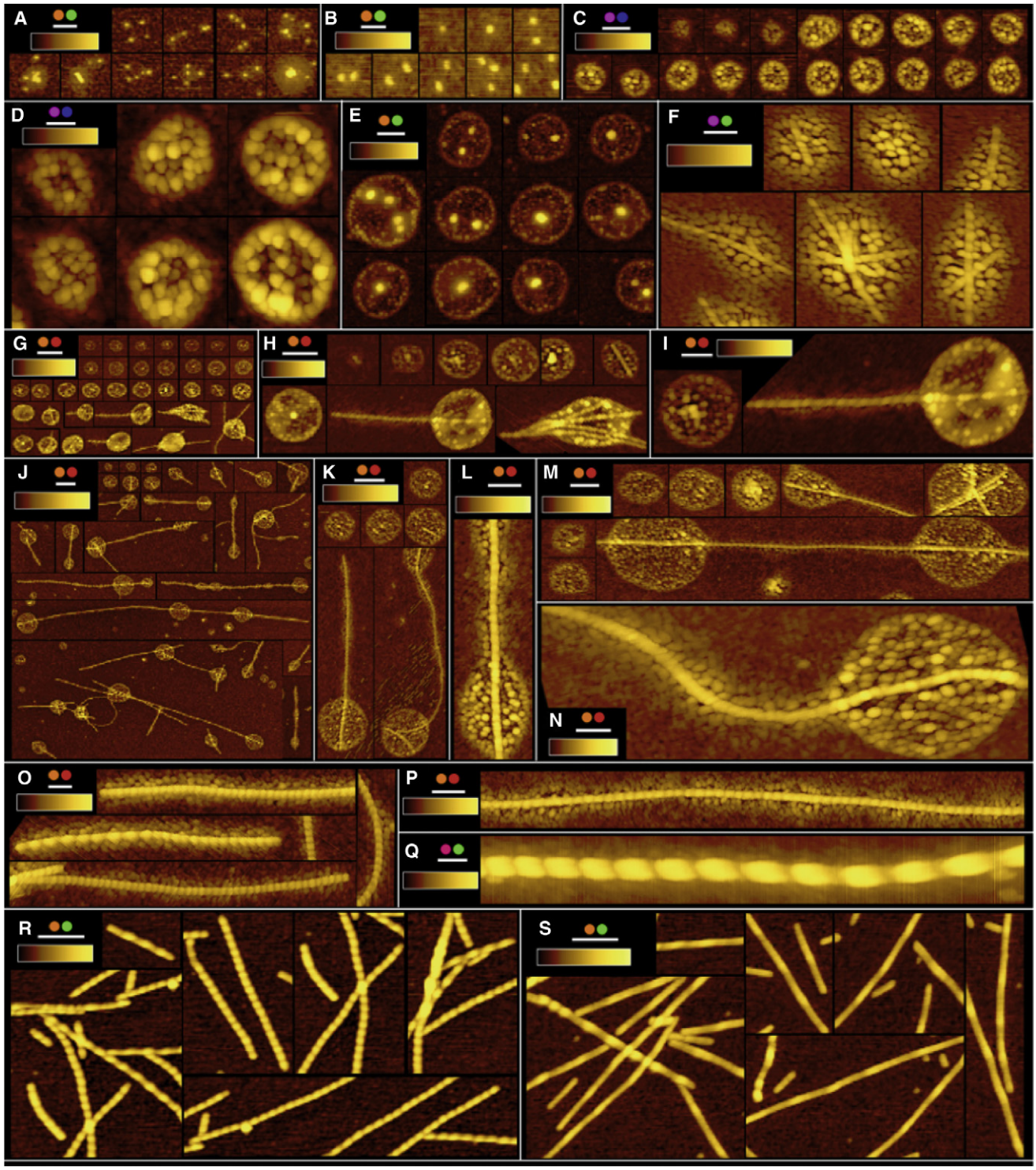

FIGURE 2 AFM images of AS aggregation intermediates. (*A* and *B*) Fuzzy balls. (*C–E*) Latent acunas. (*F–N*) Productive acunas. (*O–Q*) Fuzzy fibers. (*R*) Denuded fibers. (*S*) Mature amyloid fibrils. *xy/z* scale bars (nm): 200/10 (*A*), 100/7 (*B*), 250/20 (*C*), 100/25 (*D*), 200/35 (*E*), 100/30 (*F*), 1000/40 (*G*), 400/40 (*H*), 200/40 (*I*), 1000/40 (*J*), 500/40 (*K*), 200/20 (*L*), 300/30 (*M*), 100/20 (*N*), 200/20 (*O*), 200/20 (*P*), 100/20 (*Q*), 100/50 (*R*), and 100/50 (*S*). Coding: wtAS (*magenta solid circles*), wtAS + 2.5%AS-MFC (*orange solid circles*), 4°C (*blue solid circles*), 37°C (*green solid circles*), 70°C (*red solid circles*); in all cases 150 μM protein, 25 mM Na-PO_4 pH 6.2, 0.02% NaN_3. All samples (except *E*) were spin-coated (see Materials and Methods for details).

AFM														
Panels	A *fuzzy balls* 37 °C	C *latent acunas* 4 °C	E *latent acunas* 37 °C	H *latent acunas* 70 °C	F *productive acunas* 37 °C		G - I *productive acunas* 70 °C		Q *fuzzy fibers* 37 °C		O *fuzzy fibers* 70 °C		R *denuded fibers* 37 °C	S *mature amyloid fibrils* 37 °C
AFM	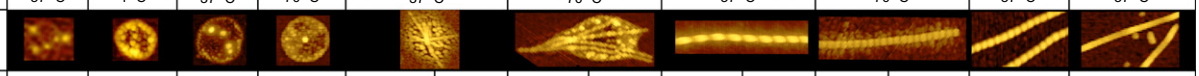													
Substructure	*core*	*core*	*core*	*core*	*core*	*fiber*	*core*	*fiber*	*fiber*	*fuzzy*	*fiber*	*fuzzy*	*fiber*	*fibril*
Height	4.5 ± 1.4	13 ± 8	25 ± 12	28 ± 15	20 ± 12	22 ± 10	27 ± 15	17 ± 11	10 ± 4	3 ± 1	13 ± 4	6 ± 3	14 ± 4	16 ± 5
Diameter	30 ± 8	240 ± 104	330 ± 74	290 ± 110	305 ± 120	31 ± 14	405 ± 88	33 ± 14	32 ± 14	45 ± 24	48 ± 18	155 ± 24	48 ± 12	49 ± 10
Period	-	-	-	-	-	39 ± 10	-	62 ± 13	150 ± 30	-	80 ± 30	-	60 ± 24	220 ± 120
P2A	-	1.2 ± 0.2	1.0 ± 0.2	1.2 ± 0.3	-		-		-		-		-	-
N	413	59	22	10	38		7		10		7		62	90

CRYO-ET			
	beaded threads	*colloidal masses*	*latent acuna*
CRYO-ET	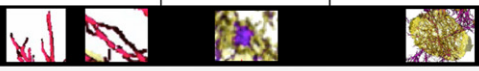		
Diameter	5.0 ± 0.5	48 ± 5	540
N	121	9	1

FIGURE 3 Dimensions of supramolecular forms of AS resolved by AFM and cryo-ET. Core refers to a central condensed structure, surrounded by a fuzzy periphery in the indicated cases. The panel designations correspond to those in Fig. 2. See Materials and Methods for other definitions and image analysis procedures. The AFM analyses were performed on 5×5 or 10×10 μm images. Note that lateral dimensions (AFM) are biased to larger values due to the influence of the finite tip diameter. For extensive characterizations of fibrillar forms of AS by AFM see Sweers et al. (50) and van Raaij et al. (51). All dimensions are given in nanometers. *N*, number of analyzed structures. Data from >10 independent reproducible experiments performed over 1.5 years.

At 37°C (Fig. 2 *E*), acunas have a more distinct rim and one to five prominent interior particles 10–20 nm in height. We ascribe a "cradle" property to these structures and denote them as *productive* because of the phenomenon evident in panels *F–N*. In samples maintained at ≥37°C under agitation, the emergence of ≥1 fibers, generally oriented symmetrically along a major axis of the acuna, can be observed. The fibers arise within the confines of the acuna (Figs. 1, *B* and *C*.3, and 2, *F–N*; for greater detail see Fig. S13 and Fig. S14) and grow, apparently by addition at both ends, emerging from the acuna and attaining a length of up to a few micrometers. These structures (denoted as fuzzy fibers, *ff*s)

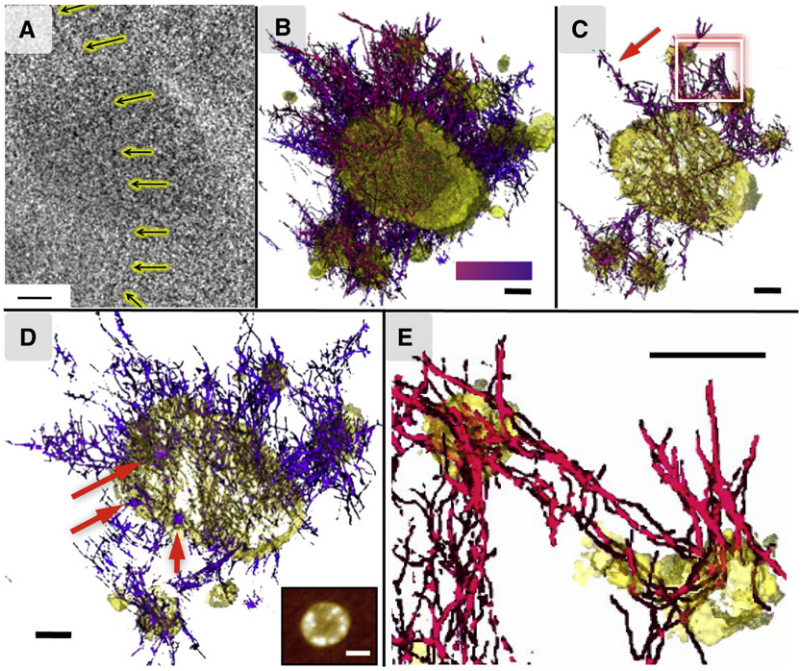

FIGURE 4 Cryo-ET of a latent acuna. (*A*) A *z*-axis slice (No. 51 of 77 slices) from a 3D tomogram of wtAS incubated at 4°C for 3 days. The arrows indicate a beaded thread traversing the acuna. (*B*) An annotated central cutaway of the same acuna (*yellow*). A network of beaded threads radiates outward from the acuna (*yellow*, *center*), forming connections with surrounding islands of AS (*yellow*), presumed to be *ff*s undergoing accretion by the acuna. The color bar indicates a *z*-axis gradation in color (*purple to red*) for the annotated beaded threads, and applies to panels *C–E*. (*C*) A 20-nm-thick section from the annotated tomogram, delineating the fibrillar interconnections between the central and surrounding masses. A zoomed view of the boxed area is shown in panel *E*. (*D*) A 200-nm thick section of the inner regions of the acuna, containing interconnected condensed colloidal masses (*purple*, indicated by the *red arrows*). Inset: an AFM image of an acuna from the same preparation; white scale bar: 300 nm. (*E*) A zoomed, edited view (*boxed area*, panel *C*) of two islands of AS (*yellow*) interconnected by beaded threads. All black scale bars: 100 nm.

are segmented (period 120–180 nm, height 10 nm, diameter 20–40 nm (core) and 20–70 nm, including fuzziness) and often curved, and their extensions beyond the border of the acuna exhibit a characteristic fuzzy lateral envelope, which in some cases is regular and in others is modulated in width. At 70°C, the *ff*s are contracted (smaller period and greater height and diameter). More detailed views are given in Fig. 2, *I*, *L–N*. In panels Fig. 2, *J*, *K*, and *M*, the linking or catenation of ≥ 2 acunas by a single long *ff*, several micrometers in length, is evident. The strong ESIPT response appears to arise at this step as well.

The reaction then proceeds to the next stage, in which the transient acunas disappear. The segmented *ff*s are released (Fig. 2, *O–Q*) and subsequently transform into denuded fibers (*df*s, panel R) that lack fuzziness and show less curvature and a substantially greater height (~15 nm) and diameter (35–60 nm), and reduced periodicity (35–85 nm; Fig. 3). The final conversion is to *maf*s (panel S) with a height of 10–20 nm, a diameter of 40–60 nm, variable periodicity (100–350 nm), and lengths that in some cases exceed 5 μm. These constitute the exclusive supramolecular species at the end of the overall reaction (72 h in Fig. 1 *A*).

We used a number of controls to validate the AFM procedures, and explored other conditions (see Supporting Material for detailed descriptions). Latent acunas required $\geq$ 200 μM AS and 3–5 days of incubation at 4°C to form, but were then stable for >1 week. Acunas that formed at 37°C (Fig. S2) but maintained thereafter at 4°C (Fig. S3) did not progress spontaneously to *ff* induction. Acunas that evaporated on mica for 30 min yielded images similar to those acquired after spin-coating, excluding the latter procedure as a source of artifactual structures (Fig. S4). A sample dilution to 7 μM protein and ~1 mM buffer led to partial or complete disruption of the acunas (Fig. S5). Dilution to 3 μM protein at a constant 2.5 mM buffer preserved the structures (Fig. S6), whereas 25 mM buffer led to the grouping of two to four acunas and the appearance of fuzziness with some surface fibrillation (Fig. S7). Washing spin-coated acunas with water released and/or disintegrated them, leaving residual depressions in the underlying monomer layer and backbones/skeletons of the nascent *ff*s (Fig. S8). AFM under liquid revealed low-resolution images of structures with the general acuna shape and size (Fig. S9). Taken together, these experiments indicate that the protein concentration and ionic strength have a significant effect on the formation, appearance, and stability of the acunas, in accordance with expectation considering the high-density packing revealed by cryo-ET (see below). Higher ionic strength promotes denser packing, probably due to electrostatic screening. Finally, latent acunas deposited on an atomically flat glass substrate were clearly discernible by AFM, excluding a direct influence of the mica on the distribution and nature of the perceived supramolecular structures (Fig. S10).

The key role of temperature in dictating the course of reaction was explored further in a two-stage experiment involving fluorescence and AFM imaging (Fig. S11 and Fig. S12). Two samples (samples 1 and 2) of 300 μM wtAS were incubated at 4°C. Sample 2 also contained 3% of labeled protein (AS140C-MFC). Emission spectra were recorded after incubation at 4°C for 5 days. Additional unlabeled protein was added to both samples, and 3% of labeled protein was added to sample 1, resulting in the same final concentration of labeled and unlabeled protein in both samples. Incubation was resumed at 37°C with agitation. A dramatic increase in fluorescence, especially of the T* band, as well as the formation of productive acunas was observed in both samples (Fig. S12, *e* and *f*). They were then maintained at 4°C for 15 days, after which the T* band diminished by 50%. Fibrils and small round structures were observed by AFM. Finally, the samples were subjected to another 2 days of incubation at 37°C, leading to an increase of the T* band to the highest levels observed in the experiment, and to the formation of long, tangled *maf*s. This experiment confirmed that 1), the labeled protein does not influence the early (or late) course of aggregation (samples 1 and 2 were indistinguishable); 2), in the reaction sequence, the protein monomer gives rise to small oligomeric structures and then to latent acunas; and 3), higher temperature is required for the formation of productive acunas, fibers, and, finally, amyloid fibrils.

Cryo-ET

Unfixed, unstained samples of latent acunas were imaged by cryo-ET, vitrified directly from solution (25). We report here initial cryo-ET data for acunas formed at 4°C for 3 days from wtAS + 2.5% AS-A140C-MFC (Fig. 4). A single structure was analyzed extensively and is featured in this report; others similar in size and contrast were evident throughout the electron microscopy grid (Fig. S15, *b* and *c*, and Fig. S16).

Fig. 4 *A* shows a single *z*-axis slice of a reconstructed 3D tomogram, revealing an acuna as a high contrast oblong object of 0.4×0.6 μm. The internal structure consists of two characteristic elements: beaded threads and condensed colloidal masses (48 $\pm$ 5 nm; Fig. 3). The acuna and its associated features are annotated in different colors, as shown in Fig. 4, *B–E*. An example of a beaded thread is highlighted by arrows in Fig. 4, *A* and *C*.

The diameter of the beads constituting the linear threads is 5.0 $\pm$ 0.5 nm, in correspondence with models of potential oligomeric structures of AS (Fig. 5). The beaded threads appear to arise from the condensed colloidal masses and form a connective network within the acuna (Fig. 4 *D*) and at its surface (Fig. 4, *C–E*).

DISCUSSION

We have established the existence of the family of acunas and related intermediates in the aggregation of AS. Their

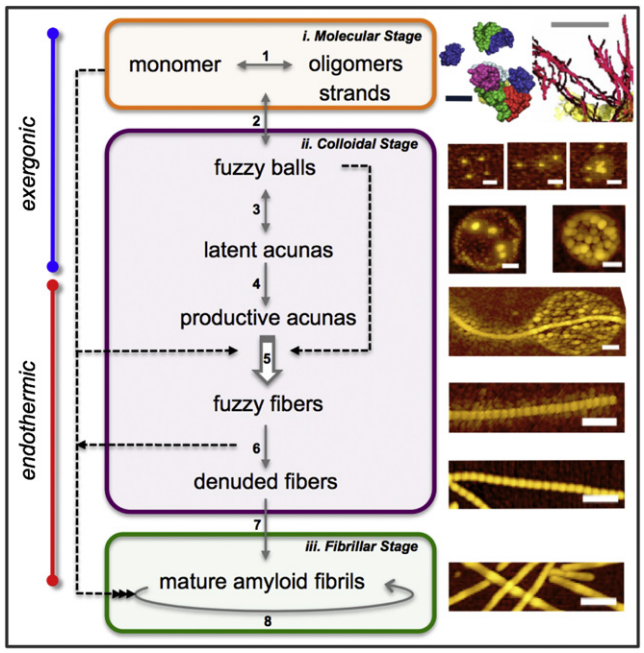

FIGURE 5 Sequential aggregation scheme (SAS) for α-synuclein. The molecular, colloidal, and fibrillar stages are depicted in terms of distinct reaction steps (*numbered*) with different degrees of reversibility (*arrows*) and of thermodynamic nature (exergonic: spontaneous reactions at low or high temperature; endothermic: reactions requiring elevated temperature). Step 1: Oligomerization (conjectural models of AS monomer, dimer, and hexamer) and end-to-end association of oligomers (*beaded threads*; cryo-ET annotated reconstruction). Step 2: Fuzzy ball condensation. Step 3: collapse to latent acunas. Step 4: Activation of productive acunas. Step 5: Generation and release of fuzzy fibers (the *open arrow* indicates a template function of the productive acunas). Step 6: Loss of fuzziness (denuded fibers) and transformation to other prefibrillar structures. Step 7: Conformational transition to the amyloid fibrillar form. Step 8: Fibrillar growth by mechanical fragmentation and terminal extension via scavenging of monomers and oligomers. Other associated processes are not shown, including 1), covalent modification (oxidation, phosphorylation, sumoylation, and ubiquitination), physiological interactions (ligands, proteins, membranes/vesicles, and organelles), PD pathological structures (Lewy bodies and neurites); 2), dehydration and ionic screening (solvent/solute) leading to alternative fibrillar mesh and amorphous precipitates; 3), cold-induced fragmentation in vitro (52); and 4), chemical inhibition and reversal of distinct steps. Cytotoxicity may originate primarily from the colloidal species. Images are not to uniform scale; scale bars: 5 nm (*black*), 100 nm (*gray* and *white*). See Fig. 2 and text for additional details.

interrelationships define a concerted sequential reaction mechanism with distinct thermodynamic and kinetic nodes. In a recent comprehensive review, Morris et al. (26) identified >18 methods for studying amyloid aggregation and proposed five mechanisms for monomer polymerization. Many of these approaches are phenomenological due to the absence of explicit knowledge about presumed intermediates such as the amyloid protofibril (27). In this study, a versatile environment-sensitive ESIPT fluorescent probe (15) enabled the detection (Fig. 1) and systematic exploration by high-resolution AFM and cryo-ET of transient species that appeared early in the reaction (Figs. 2 and 4). The two techniques in tandem revealed the size and morphology of the novel supramolecular intermediate, the latent acuna. The cryo-ET images provided high-resolution views of the vitrified entities in solution, revealing the complex internal structure of latent acunas and permitting a more accurate interpretation of the complementary topographic (surface) view supplied by AFM. We adopted an intentionally descriptive terminology for the complex, previously unreported supramolecular species to avoid confusion with terms that have generally been applied to fibrillar forms.

In accordance with Xu (28,29), we propose that AS and possibly other amyloid proteins self-associate in a manner reflecting the general properties of colloidal systems (1 nm to 1 μm in size) modulated by features conferred by the nature and sequence of the amino acid (aa) side chains. This consideration and the available experimental data lead us to propose the multistate sequential association scheme (SAS) depicted in Fig. 5. We propose a sequence of distinct structural transformations (numbered) that occur in three stages defined by the size range and nature of the species involved: 1), molecular; 2), colloidal; and 3), fibrillar. We also distinguish between the initial exergonic steps, i.e., those occurring spontaneously even at low temperature (4°C) and the subsequent endothermic steps, requiring elevated temperature (e.g., $\geq$37°C). The SAS is clearly more complex in terms of structural diversity than the three-state (monomer, oligomer, and fibril) mechanism that is generally invoked for amyloid assembly, although it fulfills the predictions based on consideration of the physical equilibria treated in such formulations (30).

The molecular stage of aggregation (Fig. 5, step 1) involves monomeric and oligomeric states of AS. Although AS is generally regarded as an intrinsically disordered protein, according to NMR/MS data (31,32), it adopts a compact (~5 nm) spherical or ellipsoidal structure in solution. Regardless of the particular fold of an individual AS monomer, the asymmetrical distribution of charged amino acids gives rise to a strong dipole moment. AS exhibits a pronounced tendency to form stable dimers (32,33) and higher-order oligomeric species. A recent study suggested that AS may exist physiologically in a tetrameric, α-helical aggregation-resistant form (34). Although this finding remains to be confirmed, it is evident that pauci-oligomeric-associated states of AS constitute the building blocks of the filamentous and condensed features revealed by cryo-ET and AFM.

The colloidal stage (steps 2–6) comprises the compaction of the discrete AS oligomeric and filamentous forms into particles (*fb*s). We propose that the condensed colloidal masses seen by cryo-ET and AFM originate from the *fb*s, and that the beaded threads constitute the fuzziness identified by AFM, presumably stabilizing the supramolecular structure and recruiting material from the periphery.

According to the linear colloidal aggregation model proposed by Xu (28,29), aggregation of molecules into colloidal particles is driven by surface energy minimization resulting from compensation of long-range charge-charge and short-range van der Waals interactions. Specific site-site or structure-structure interactions may not be involved.

Because of the omnidirectionality of the operative forces, the colloidal particles are spherical and remain in suspension due to intrinsic + adsorbed charge and surface potential. However, inherent attractive interactions must exist, in view of the accretion zones and ultimate condensation into the supramolecular acunas. That is, the fuzziness observed by AFM in numerous intermediates constitutes a type of molecular Velcro, corresponding to the fine beaded threads revealed by cryo-ET as a matrix interlinking the globular masses of more densely packed oligomers (Fig. 4).

Agitation and elevated temperature (e.g., 37°C) are required for progression to the next and perhaps most critical step (5) (Fig. 5), the generation of productive acunas and extrusion of linear aggregates, the *ff*s. After efficient nucleation on the productive acunas, linear growth is presumed to progress by catenation of *fb*s, perhaps with the participation of other free oligomeric forms. The acunas may facilitate conformational rearrangements in a manner reminiscent of chaperones. For example, a nonclassical (physiological?) chaperone activity of AS in the maintenance of presynaptic SNARE-complexes has been reported (35). The strong ESIPT signal is indicative of a reduced polarity in the immediate microenvironment of the probe, from which we infer that the surrounding structure is more condensed and less exposed to the aqueous medium. The directionality of growth is rationalized by a key feature of the linear colloidal aggregation model: the appearance of an asymmetric charge distribution leading to a finite dipole moment in the colloidal spheroids. A possible mechanism for generating the required dipole-dipole asymmetry (29) is the formation of α-sheet secondary structure, proposed by numerous investigators (29,36–39) as a transient phase in protein amyloidosis. In the α-sheet configuration, all of the NH groups are on one side and all of the carbonyl groups are on the other side of the polypeptide strand. Shape complementarity (40) may also confer specificity to this process.

Free *ff*s arise from and at the cost of the productive acunas, which disappear. The modulations and multiple attachments depicted in Figs. 1 *B* and 2, *J* and *M*, suggest that *ff* catenates may themselves serve as accretion centers as they grow, generating secondary acunas. The *ff*s then evolve into *maf*s via intermediate denuded fibers (*df*s), which are distinguishable by their lack of fuzziness (Fig. 2 *R*). We propose that fuzziness is an inherently dynamic, tenuous property that reflects the general colloidal state of the system as well as the protein identity, i.e., the primary sequence. Although fuzziness survives moderate degrees of isotonic dilution, it is lost upon centrifugation or size-exclusion chromatography of *fb*s and *ff*s. These procedures, which are often used in the fractionation of amyloid oligomers, lower the free protein concentration. Considering that the subsequent step of fibrillization does the same (see below), we conclude that fuzziness reflects the noncovalent association of AS monomer and/or oligomers with a catenated fiber core. Thus, it appears that *ff*s have little relation to the fuzzy coat of tau fibrils, which is not visualized by AFM and is an integral part of the core protein, being released only by proteolysis (41). A recent study of prefibrillar intermediates of wtAS aggregation, seeded by an aggregation-incompetent triple mutant A30P/A56P/A76P (TP aS), featured electron microscopy images very reminiscent of *ff*s (see Fig. 2 A of Karpinar et al. (42)).

The fibrillar stage (SAS, steps 7 and 8) is unique in many respects, the most conspicuous of which is the concerted transition in the secondary structure of the *ff*s (via *df*s) to the cross-β-sheet conformation constituting the cross-sectional element of the amyloid fibril (*maf*). Xu (29) provided a detailed description of a proposed α-sheet to cross-β-sheet transition based on theoretical and experimental considerations. Such a transformation could nucleate internally or terminally in the fiber under the influence of small variations in the concentrations of effector molecules. This is an attractive hypothesis with regard to disease evolution as well as the design of therapeutic strategies. Templated conformational change may also play a role (43). Once the *maf*s emerge, they supplant the preceding acuna-dependent growth mechanism by propagation via mature amyloid reactive sites. The rapid addition of monomer and/or oligomeric AS units (e.g., stable dimers (32,33)) is very efficient (26) in scavenging the monomer and thereby displacing the dynamic equilibria of the acuna manifold (preamyloid steps 1–6) back to the monomeric and oligomeric states. In this respect, the stage of fibrillar growth short-circuits the system and renders it largely irreversible, such that the final reaction products in vitro and possibly in vivo (44) are *maf*s and residual, depleted monomer-oligomer. Of course, such a scenario applies only to a reaction triggered as a unique synchronous event. In the more likely continuous steady-state process applicable in the cell, including in the context of PD, all species of the SAS would be represented in the AS population distribution.

Of the numerous noncanonical features of the proposed mechanism for the aggregation of AS, distinct from that of Aβ (45), the most significant is that neurotoxicity may primarily involve soluble, molecular species that lack the amyloid features characteristic of the classical *maf*s (46), notably a cross-β-sheet secondary structure and the tendency to form an entangled network. Acunas and *ff*s exhibit great potential for toxic gain-of-function given their inherently complex surface structure, and the influence of multiple influences in the cellular context. These include AS concentration and modification(s), and

interactions with other proteins, membranes, compartments, and organelles.

The acuna entities may also serve as key elements of other amyloid protein systems. A recent study of Aβ peptide self-assembly (47) featured fluorescence images that may correspond to AS acunas, and AFM images of amyloidogenic yeast Sup35 aggregation intermediates are reminiscent of the highly segmented *ff*s (48). We surmise that acunas have previously eluded detection due to 1), their transient nature; 2), their low fractional concentration (estimated by preliminary ultracentrifugation analysis as $<$20% at the acuna stage); 3), the requirement for a high protein concentration; and 4), the use of destabilizing AFM washing protocols. A major challenge raised by this study is the need to devise a means of fractionating the molecular species represented in Fig. 5 so as to determine their interactomes, toxicities, and antigenicities (6). In the event that the latter are strong and specific, prophylactic and/or therapeutic vaccination strategies for preventing or reversing the disease state are conceivable. In parallel, one could screen for selective agents (49) capable of reducing the load of specific neurotoxic species, either directly or by inhibiting the entry or facilitating the exit from their respective reaction compartments (Fig. 5).

SUPPORTING MATERIAL

Additional materials and methods, 17 figures, and references (53–56) are available at http://www.biophysj.org/biophysj/supplemental/S0006-3495(12)00168-3.

We thank R. Klement for providing the molecular models of oligomeric α-depicted in Fig. 5; V. Subramaniam and I. Segers-Nolten (University of Twente, The Netherlands) for conducting confirmatory AFM measurements; and Jason Hafner at Rice University for providing the AFM equipment used to assay the specimen in parallel with the cryo-ET experiments.

This work was supported by the Max Planck Society (T.J. and E.J.-E.), the Max Planck Toxic Protein Conformation project, and the Cluster of Excellence 171 of the DFG Center for the Molecular Physiology of the Brain. E.J.-E. received support from the Argentine agencies ANpCyT, CONICET, and the University of Buenos Aires. J.F. received support from CONICET and the University of Buenos Aires. D.Y. received a fellowship from the Marie Curie Foundation. W.C. and S.S. received grants from the National Institutes of Health (P41RR002250 and PN2EY016525). S.S. was supported by a training fellowship from the Nanobiology Interdisciplinary Graduate Training Program of the W.M. Keck Center for Interdisciplinary Bioscience Training of the Gulf Coast Consortia (NIH grant No. T32EB009379).

REFERENCES

1. Chiti, F., and C. M. Dobson. 2006. Protein misfolding, functional amyloid, and human disease. *Annu. Rev. Biochem.* 75:333–366.
2. Uversky, V. N. 2008. α-Synuclein misfolding and neurodegenerative diseases. *Curr. Protein Pept. Sci.* 9:507–540.
3. Jellinger, K. A. 2010. Basic mechanisms of neurodegeneration: a critical update. *J. Cell. Mol. Med.* 14:457–487.
4. De Meyer, G., F. Shapiro, …, J. Q. Trojanowski, Alzheimer's Disease Neuroimaging Initiative. 2010. Diagnosis-independent Alzheimer disease biomarker signature in cognitively normal elderly people. *Arch. Neurol.* 67:949–956.
5. Vekrellis, K., M. Xilouri, …, L. Stefanis. 2011. Pathological roles of α-synuclein in neurological disorders. *Lancet Neurol.* 10:1015–1025.
6. Uversky, V. N. 2010. Mysterious oligomerization of the amyloidogenic proteins. *FEBS J.* 277:2940–2953.
7. Stefani, M. 2010. Structural polymorphism of amyloid oligomers and fibrils underlies different fibrillization pathways: immunogenicity and cytotoxicity. *Curr. Protein Pept. Sci.* 11:343–354.
8. Stefani, M. 2010. Protein aggregation diseases: toxicity of soluble prefibrillar aggregates and their clinical significance. *Methods Mol. Biol.* 648:25–41.
9. Armstrong, R. A., P. L. Lantos, and N. J. Cairns. 2008. What determines the molecular composition of abnormal protein aggregates in neurodegenerative disease? *Neuropathology.* 28:351–365.
10. Malkus, K. A., E. Tsika, and H. Ischiropoulos. 2009. Oxidative modifications, mitochondrial dysfunction, and impaired protein degradation in Parkinson's disease: how neurons are lost in the Bermuda triangle. *Mol. Neurodegener.* 4:24.
11. Bertoncini, C. W., and M. S. Celej. 2011. Small molecule fluorescent probes for the detection of amyloid self-assembly *in vitro* and *in vivo*. *Curr. Protein Pept. Sci.* 12:205–220.
12. Lindgren, M., and P. Hammarström. 2010. Amyloid oligomers: spectroscopic characterization of amyloidogenic protein states. *FEBS J.* 277:1380–1388.
13. Klymchenko, A. S., and A. P. Demchenko. 2008. Multiparametric probing of microenvironment with solvatochromic fluorescent dyes. *Methods Enzymol.* 450:37–58.
14. Celej, M. S., W. Caarls, …, T. M. Jovin. 2009. A triple-emission fluorescent probe reveals distinctive amyloid fibrillar polymorphism of wild-type α-synuclein and its familial Parkinson's disease mutants. *Biochemistry.* 48:7465–7472.
15. Yushchenko, D. A., J. A. Fauerbach, …, T. M. Jovin. 2010. Fluorescent ratiometric MFC probe sensitive to early stages of α-synuclein aggregation. *J. Am. Chem. Soc.* 132:7860–7861.
16. Dierksen, K., D. Typke, …, W. Baumeister. 1995. Three-dimensional structure of lipid vesicles embedded in vitreous ice and investigated by automated electron tomography. *Biophys. J.* 68:1416–1422.
17. Grimm, R., H. Singh, …, W. Baumeister. 1998. Electron tomography of ice-embedded prokaryotic cells. *Biophys. J.* 74:1031–1042.
18. Moritz, M., M. B. Braunfeld, …, D. A. Agard. 1995. Three-dimensional structural characterization of centrosomes from early Drosophila embryos. *J. Cell Biol.* 130:1149–1159.
19. Gilkey, J. C., and A. Staehelin. 1986. Advances in ultra-rapid freezing for preservation of cellular ultrastructure. *J. Electron Microsc. Tech.* 3:177–210.
20. Kellenberger, E., R. Johansen, …, W. Villiger. 1992. Artefacts and morphological changes during chemical fixation. *J. Microsc.* 168:181–201.
21. Dubochet, J., M. Adrian, …, P. Schultz. 1988. Cryo-electron microscopy of vitrified specimens. *Q. Rev. Biophys.* 21:129–228.
22. Kremer, J. R., D. N. Mastronarde, and J. R. McIntosh. 1996. Computer visualization of three-dimensional image data using IMOD. *J. Struct. Biol.* 116:71–76.
23. Tang, G., L. Peng, …, S. J. Ludtke. 2007. EMAN2: an extensible image processing suite for electron microscopy. *J. Struct. Biol.* 157:38–46.
24. Pelah, A., T. M. Jovin, and I. Szleifer. 2007. Diverse two-dimensional arrays of PNIPAM Beads formed by spin-coating. *Colloid. Surface. A.* 299:1–7.
25. Koning, R. I., and A. J. Koster. 2009. Cryo-electron tomography in biology and medicine. *Ann. Anat.* 191:427–445.

26. Morris, A. M., M. A. Watzky, and R. G. Finke. 2009. Protein aggregation kinetics, mechanism, and curve-fitting: a review of the literature. *Biochim. Biophys. Acta.* 1794:375–397.

27. Lashuel, H. A., and P. T. Lansbury, Jr. 2006. Are amyloid diseases caused by protein aggregates that mimic bacterial pore-forming toxins? *Q. Rev. Biophys.* 39:167–201.

28. Xu, S. 2007. Aggregation drives "misfolding" in protein amyloid fiber formation. *Amyloid.* 14:119–131.

29. Xu, S. 2009. Cross-β-sheet structure in amyloid fiber formation. *J. Phys. Chem. B.* 113:12447–12455.

30. Schmit, J. D., K. Ghosh, and K. Dill. 2011. What drives amyloid molecules to assemble into oligomers and fibrils? *Biophys. J.* 100:450–458.

31. Bertoncini, C. W., Y.-S. Jung, …, M. Zweckstetter. 2005. Release of long-range tertiary interactions potentiates aggregation of natively unstructured α-synuclein. *Proc. Natl. Acad. Sci. USA.* 102:1430–1435.

32. Frimpong, A. K., R. R. Abzalimov, …, I. A. Kaltashov. 2010. Characterization of intrinsically disordered proteins with electrospray ionization mass spectrometry: conformational heterogeneity of α-synuclein. *Proteins.* 78:714–722.

33. Yu, J., and Y. L. Lyubchenko. 2009. Early stages for Parkinson's development: α-synuclein misfolding and aggregation. *J. Neuroimmune Pharmacol.* 4:10–16.

34. Bartels, T., J. G. Choi, and D. J. Selkoe. 2011. α-Synuclein occurs physiologically as a helically folded tetramer that resists aggregation. *Nature.* 477:107–110.

35. Burré, J., M. Sharma, …, T. C. Südhof. 2010. α-Synuclein promotes SNARE-complex assembly in vivo and in vitro. *Science.* 329:1663–1667.

36. Daggett, V. 2006. α-Sheet: the toxic conformer in amyloid diseases? *Acc. Chem. Res.* 39:594–602.

37. Hayward, S., and E. J. Milner-White. 2008. The geometry of α-sheet: implications for its possible function as amyloid precursor in proteins. *Proteins.* 71:415–425.

38. Milner-White, J. E., J. D. Watson, …, S. Hayward. 2006. Amyloid formation may involve α- to β-sheet interconversion via peptide plane flipping. *Structure.* 14:1369–1376.

39. Wu, H., A. Canfield, …, S. Huo. 2010. Quantum mechanical studies on model α-pleated sheets. *J. Comput. Chem.* 31:1216–1223.

40. Macfarlane, R. J., and C. A. Mirkin. 2010. Colloidal assembly via shape complementarity. *ChemPhysChem.* 11:3215–3217.

41. Wegmann, S., Y. J. Jung, S. Chinnathambi, E.-M. Mandelkow, E. Mandelkow, and D. J. Muller. 2010. Human Tau isoforms assemble into ribbon-like fibrils that display polymorphic structure and stability. *J. Biol. Chem.* 285:27302–27313.

42. Karpinar, D. P., M. B. Balija, …, M. Zweckstetter. 2009. Pre-fibrillar α-synuclein variants with impaired β-structure increase neurotoxicity in Parkinson's disease models. *EMBO J.* 28:3256–3268.

43. Frost, B., J. Ollesch, …, M. I. Diamond. 2009. Conformational diversity of wild-type Tau fibrils specified by templated conformation change. *J. Biol. Chem.* 284:3546–3551.

44. Ossato, G., M. A. Digman, …, E. Gratton. 2010. A two-step path to inclusion formation of huntingtin peptides revealed by number and brightness analysis. *Biophys. J.* 98:3078–3085.

45. Chimon, S., M. A. Shaibat, …, Y. Ishii. 2007. Evidence of fibril-like β-sheet structures in a neurotoxic amyloid intermediate of Alzheimer's β-amyloid. *Nat. Struct. Mol. Biol.* 14:1157–1164.

46. Apetri, M. M., N. C. Maiti, …, V. E. Anderson. 2006. Secondary structure of α-synuclein oligomers: characterization by raman and atomic force microscopy. *J. Mol. Biol.* 355:63–71.

47. Liang, Y., D. G. Lynn, and K. M. Berland. 2010. Direct observation of nucleation and growth in amyloid self-assembly. *J. Am. Chem. Soc.* 132:6306–6308.

48. Xu, S., B. Bevis, and M. F. Arnsdorf. 2001. The assembly of amyloidogenic yeast sup35 as assessed by scanning (atomic) force microscopy: an analogy to linear colloidal aggregation? *Biophys. J.* 81:446–454.

49. Lamberto, G. R., A. Binolfi, …, C. O. Fernández. 2009. Structural and mechanistic basis behind the inhibitory interaction of PcTS on α-synuclein amyloid fibril formation. *Proc. Natl. Acad. Sci. USA.* 106:21057–21062.

50. Sweers, K., K. van der Werf, …, V. Subramaniam. 2011. Nanomechanical properties of α-synuclein amyloid fibrils: a comparative study by nanoindentation, harmonic force microscopy, and Peakforce QNM. *Nanoscale Res. Lett.* 6:270.

51. van Raaij, M. E., J. van Gestel, …, V. Subramaniam. 2008. Concentration dependence of α-synuclein fibril length assessed by quantitative atomic force microscopy and statistical-mechanical theory. *Biophys. J.* 95:4871–4878.

52. Kim, H.-Y., M.-K. Cho, …, M. Zweckstetter. 2009. Structural properties of pore-forming oligomers of α-synuclein. *J. Am. Chem. Soc.* 131:17482–17489.

53. Thirunavukkuarasu, S., E. A. Jares-Erijman, and T. M. Jovin. 2008. Multiparametric fluorescence detection of early stages in the amyloid protein aggregation of pyrene-labeled α-synuclein. *J. Mol. Biol.* 378:1064–1073.

54. Starink, J. P. P., and T. M. Jovin. 1996. Background correction in scanning probe microscope recordings of macromolecules. *Surf. Sci.* 359:291–305.

55. Ermantraut, E., K. Wohlfart, and W. Tichelaar. 1998. Perforated support foils with predefined hole size, shape and arrangement. *Ultramicroscopy.* 74:75–81.

56. Mastronarde, D. 2003. SerialEM. A program for automated tilt series acquisition on Tecnai microcopes using prediction of specimen position. *Microsc. Microanal.* 9:1182–1183.